COMPEL
45,4

Received 28 October 2025
Revised 20 December 2025
Accepted 3 February 2026

Surrogate-based optimization of coupled inductors

Christian Riener
Division Power Electronics, Silicon Austria Labs GmbH, Graz, Austria

Simon Sawatzki
Vacuumschmelze GmbH und Co KG, Hanau, Germany

Mehtab Hussain
Division Power Electronics, Silicon Austria Labs GmbH, Graz, Austria

Patrick Dominik Gsoels
Division Power Electronics, Silicon Austria Labs GmbH, Graz, Austria; Christian Doppler Laboratory for EMC Aware Robust Electronic Systems, Graz, Austria and Institute of Electronics, Graz University of Technology, Graz, Austria, and

Martin Stoiber and Jose Romero Lopera
Division Power Electronics, Silicon Austria Labs GmbH, Graz, Austria

Abstract

Purpose – The purpose of this paper is to present an application-specific optimization methodology for the design of coupled inductors used in multilevel interleaved power converters. This study focuses on minimizing core losses to meet power density requirements, reducing component volume to address cost constraints and maximizing longitudinal inductance to enhance electromagnetic interference (EMI) performance.

Design/methodology/approach – A multiobjective optimization (MOO) approach based on the NSGA-II algorithm is used to determine the Pareto-optimal design of the coupled inductor that satisfies the target power rating of 120 kW while minimizing volume for improved cost-effectiveness. The optimization incorporates key functional parameters, including main inductance, core losses and coil leakage inductance, the latter serving as an element for EMI filtering. To efficiently address the MOO problem, analytical models of the main inductance and core losses are integrated with a surrogate model of the device under test leakage inductance, derived from 2.5D finite element simulations.

Findings – Three Pareto-optimal designs are evaluated against a commercial reference in terms of core losses, inductance and cost. The low-loss design minimizes losses but requires a core twice as large as the reference, increasing cost by 60%. The compact design cuts material use by an order of magnitude but leads to substantially higher losses. The high-inductance design more than doubles inductance yet demands the largest core, raising cost by 70%. These results highlight a clear trade-off between magnetic efficiency, inductive performance and cost-effectiveness.

COMPEL - The international journal for computation and mathematics in electrical and electronic engineering
Vol. 45 No. 4, 2026
pp. 674-689
Emerald Publishing Limited
0332-1649
DOI 10.1108/COMPEL-10-2025-0495

Research limitations/implications – This study is limited by practical factors affecting manufacturability and performance. The proposed designs require complex multilayer windings that increase leakage inductance, parasitics and fabrication difficulty. Winding capacitance and thermal effects are not modeled, though both significantly impact high-frequency and high-loss operation. Assumed filling factors may not reflect real winding technologies, affecting packing density and losses. Moreover, the smallest-volume designs may demand extra cooling, reducing practical benefits. Future work should include detailed winding models, parasitic capacitance and coupled thermal–electromagnetic analysis to better capture real-world performance and reliability.

Practical implications – The proposed methodology provides a quantitative framework to support informed trade-off decisions between key functional parameters – such as loss efficiency, inductance and space utilization – while also addressing EMI-related aspects and ensuring economic competitiveness.

Originality/value – The novelty of this work lies in its integrated optimization workflow for coupled inductor design, which simultaneously accounts for key functional parameters – such as efficiency, inductance and space utilization – while incorporating EMI-related factors and cost considerations within a unified framework.

Keywords Blackbox optimization, Coupled inductors, Gaussian process regression, Surrogate model, Multiobjective optimization

Paper type Research paper

Introduction

The ongoing trend toward higher switching frequencies, increased functional integration and greater power densities has made it more challenging to achieve the necessary power ratings and electromagnetic compatibility (EMC) compliance in AC–DC power converters. Advancements into the sub-megahertz (MHz) switching frequency range and beyond (Mohammed and Jung, 2021) enable significant reductions in the size of inductive components, e.g. coupled inductors that use ferromagnetic materials (Rashid, 2024), thereby lowering costs and enhancing power density. However, higher operating frequencies lead to increased electromagnetic emissions within the conducted emission band (Paul, 2006), thus requiring additional filtering stages, such as common-mode chokes, to comply with regulatory limits. These additional components counteract the reductions in size and cost, creating an inherent trade-off between compactness and EMC performance. Addressing this trade-off is essential for developing competitive, high-performance power conversion solutions.

The literature presents a wide range of design approaches for inductive components in AC–DC power converters. In (Rashid, 2024) and (Cheng *et al.*, 2022), analytical methods based on magnetic circuit theory are used to design inductive components, including the determination of core reluctance. Another methodology uses behavioral models derived from circuit simulations and fitted to transient measurement data, as shown in Oliveri *et al.* (2022). Finite element (FE) simulation-based approaches are reported in Abarzadeh *et al.* (2023) and Mirza *et al.* (2023), where the Ansys toolchain is applied to the design process. A comprehensive survey of modeling techniques with varying levels of complexity for magnetic components is provided in Górecki and Detka (2023). While these methods offer valuable insights, they primarily address functional parameters such as power ratings, saturation behavior and thermal performance. In contrast, this work considers essential functional aspects, as well as commercially relevant factors such as component volume and cost, to identify a set of feasible designs that balance performance with economic competitiveness.

The device under test (DUT) is a coupled inductor (CI), which is used in a multilevel interleaved power converter (Anderson *et al.*, 2017) rated at 120 kW, with the converter topology shown in Figure 1. The CI uses a nanocrystalline toroidal core (Vacuumschmelze,

2025), and its geometric features are shown in Figure 2. The main inductance of each coil is denoted as L_{base}, while L_{long} represents the longitudinal inductance (Boillat and Kolar, 2012). As shown in Zhang *et al.* (2010), the longitudinal inductance is beneficial for electromagnetic interference (EMI) suppression when used in an EMI filter. This inductance can be realized either by a dedicated inductor or by exploiting the leakage inductance of the two coils. The latter approach offers a significant advantage by reducing the required volume, decreasing the amount of ferromagnetic material needed and lowering costs. Thus in this work, the CI is designed such that the necessary longitudinal inductance is achieved through coil leakage.

A multiobjective optimization (MOO) strategy is used to find a design of the CI that meets the required power ratings (here 120 kW) while minimizing volume for cost-effectiveness. This optimization strategy considers functional parameters, such as the main inductance L_{base} and core losses, as well as the coil's leakage inductances, to achieve the necessary L_{long} for EMI filtering. To efficiently solve the MOO problem, analytical models of L_{base} and core losses (Möreé and Leijon, 2024) are combined with a surrogate model of the longitudinal inductance L_{long} developed from 2.5D FE simulations.

Modeling

The DUT is a toroidal-shaped coupled inductor, with its cross sections and input parameters $\mathbf{x} = [x_0, \ldots, x_5]$ shown in Figure 2. Assuming that the nanocrystalline core exhibits isotropic and linear magnetic behavior, and that the magnetic flux is uniformly confined within the core, the inductance L_{base}, can be approximated using Ampere's law as follows (Hurley *et al.*, 2025):

$$L_{base}(\mathbf{x}) = \frac{\mu_0 \mu_r x_1 x_2 x_3^2}{2\pi\left(x_0 + \frac{x_1}{2}\right)} \tag{1}$$

where μ_0 is the permeability of free space and μ_r is the relative permeability of the nanocrystalline core. The input parameters x_0, x_1, x_2 are the inner core radius, core width and core height (see Figure 2), while x_3 represents the number of turns of one coil.

The core losses are estimated based on Steinmetz's equation (Möreé and Leijon, 2024) as follows:

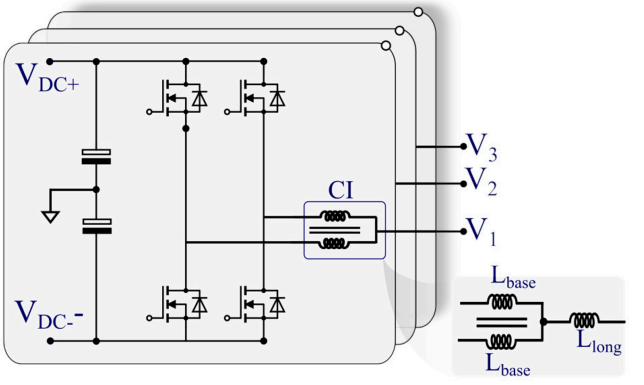

Figure 1. Multilevel interleaved power converter

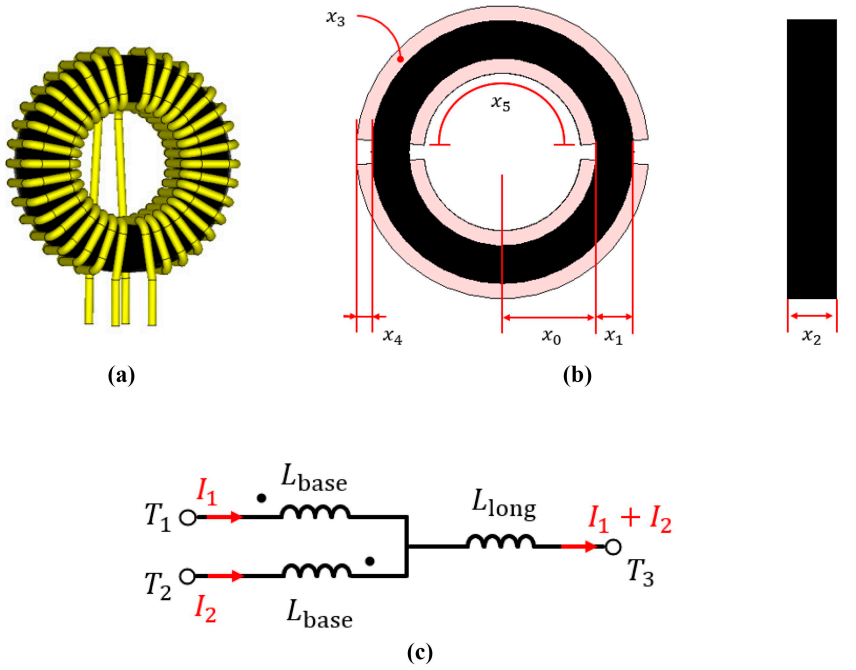

Figure 2. (a) Investigated DUT and (b) cross sections (front-view and side-view) with the input parameters $\mathbf{x} = [x_0, \ldots, x_5]$ of the model. The parameters x_0, x_1, x_2 are the geometric features of the core while x_3, x_4, x_5 represent the number of turns, the thickness and the coverage of one coil. (c) equivalent circuit model of the DUT, where L_{base} models the main inductance of a coil and L_{long} is the longitudinal inductance (Boillat and Kolar, 2012)

$$P_{\text{core, loss}}(\mathbf{x}) = P_0 V_{\text{core}}(\mathbf{x}) \left(\frac{f}{f_0}\right)^a \left(\frac{B(\mathbf{x})}{B_0}\right)^b \tag{2}$$

where P_0 is the nominal core loss provided in the material datasheet (Vacuumschmelze, 2025) for a given frequency f_0 and magnetic flux density B_0. The corresponding values of P_0, f_0 and B_0 are summarized in Table 1. The parameter V_{core} is the core volume, defined as:

Table 1. Parameter values for estimating L_{base} in (1), $P_{\text{core, loss}}$ in (2) and B in (4)

μ_r	P_0	f_0	B_0	a	b
[1]	[W/kg]	[kHz]	[T]	[1]	[1]
4000	80	100	0.3	1.5	2.4

Note(s): The given values are obtained from the datasheet (Vacuumschmelze, 2025) or directly from the manufacturer

$$V_{\text{core}}(\mathbf{x}) = 2\pi\left(x_0 + \frac{x_1}{2}\right)x_1x_2. \tag{3}$$

The parameter f is the switching frequency and B is the magnitude of the magnetic flux density within the core defined as follows (Hurley *et al.*, 2025):

$$B(\mathbf{x}) = \frac{\mu_0\mu_r x_3 I_T(\mathbf{x})}{\pi\left(x_0 + \frac{x_1}{2}\right)} \tag{4}$$

where I_T is the DUT's transverse current defined as $I_T(\mathbf{x}) = I_1 - I_2$ [see Figure 2(c)]. Figure 3(a) shows the transient switched node voltage V_{sw} connected between the terminals T_1 and T_2 of the DUT and the resulting current I_T. Applying fundamental circuit theory (Hufschmied, 2020), I_T can be obtained as follows:

$$I_T(\mathbf{x}) = \frac{1}{4L_{base}(\mathbf{x})}\int_0^T V_{sw}(t)\,dt \tag{5}$$

where $4L_{base}(\mathbf{x})$ describes the transverse inductance of the DUT (assuming perfect coupling between the two coils) and T is the duration of the fundamental period of V_{sw}.

Finally, the Fast Fourier Transform of I_T yields its spectral components, as shown in Figure 3(b). The Steinmetz equation in (2) assumes a sinusoidal excitation (Möreé and Leijon, 2024). However, Figure 3(b) illustrates that the excitation current exhibits a predominantly triangular waveform. Consequently, using the Steinmetz equation introduces an estimated error of approximately 10% (see Appendix). Because the primary focus of this paper is the optimization workflow rather than high-fidelity core-loss modeling, this level of accuracy is considered acceptable.

To determine the longitudinal inductance L_{long} of the DUT [see Figure 2(c)], 2.5D magneto-static FE simulations have been carried out in CST Studio Suite (Dassault Systèmes, 2025). A simplified coil model has been used, considering a homogeneous source current density across the coil cross section, such that the magnetic flux generated by the coil is proportional to the number of turns (Dassault Systèmes, 2025). The prescribed current

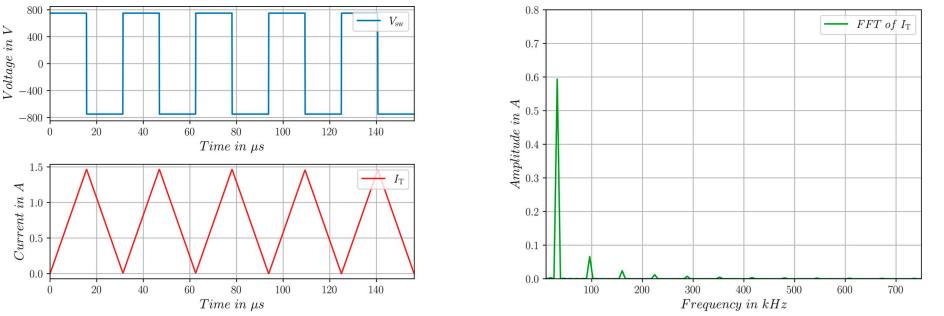

(a) **(b)**

Figure 3. (a) Switched voltage V_{sw} across DUT terminals T_1 and T_2 in Figure 2(c), operated at a switching frequency of 34 kHz, along with the corresponding transverse current I_T through the DUT; and (b) spectral components of I_T in (a)

direction, along with the resulting magnetic flux density and magnetic energy density, is illustrated in Figure 4. As shown, the transverse magnetic flux generated by the two coils within the core material effectively cancels each other out [see Figure 4(c)], resulting in a negligible main inductance L_{base}. Consequently, the longitudinal inductance can be determined as follows:

$$L_{\text{long}} = \frac{2w_{\text{mag}}}{I_L^2} \tag{6}$$

where w_{mag} is the magnetic energy density obtained from FE simulations [see Figure 4(d)]. The parameter I_{L} describes the excitation current and it is defined as:

$$I_L = I_1 + I_2. \tag{7}$$

For simplicity $I_{\text{L}} = 1$ A has been chosen.

The 2.5D FE simulation model used in this paper requires approximately 2 s (using 16 CPU cores on a HPC cluster) to compute L_{long}, hence its computational complexity is very low, if only single input parameter combinations are of interest. However, when the FE model for L_{long} is combined with analytical models for L_{base} and $P_{\text{core, loss}}$ in the context of an MOO problem – where several thousand evaluations are typically required – using FE simulations becomes computationally impractical. To address this, a surrogate modeling approach is introduced in the following section to significantly reduce the computational cost of estimating L_{long}, enabling the MOO problem to be solved within a feasible time frame.

Surrogate modeling

As already shown in Figure 2, the design space explored in this paper consists of $n = 6$ input parameters $\mathbf{x} = [x_0, \ldots, x_5]$, where x_0, x_1, x_2 describe various geometric features of the DUT, while x_3, x_4, x_5 represent the number of turns, the thickness and the coverage of one coil. To generate the training data set for the surrogate model, Latin Hypercube Sampling (LHS) was applied using $m = 500$ input parameter combinations, uniformly distributed across the ranges specified in Table 2. The sample size is selected according to the taxonomy of surrogate modeling methods recommended in Forrester *et al.* (2008). In addition, 50 test samples were generated using LHS to test the model's accuracy.

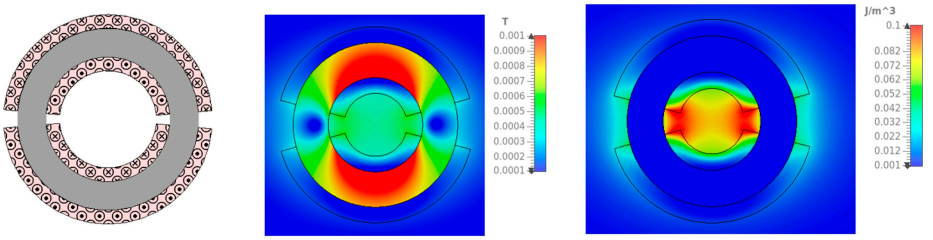

Figure 4. (a) Current excitation of the 2.5D FE model; (b) simulated magnitude of the magnetic flux density using the current excitation in (a); and (c) simulated magnetic energy density using the current excitation shown in (a)

Table 2. Bounds of design space **x**

$[l_0, u_o]$	$[l_1, u_1]$	$[l_2, u_2]$	$[l_3, u_3]$	$[l_4, u_4]$	$[l_5, u_5]$
[5, 149] mm	[6, 150] mm	[5, 30] mm	[2, 25]	[1, 10] mm	[90, 179]°

A surrogate model is constructed using Gaussian Process Regression with an isotropic rational quadratic kernel defined as (Pedregosa *et al.*, 2011):

$$k(x_i, x_j) = \left(1 + \frac{d(x_i, x_j)^2}{2\alpha l^2}\right)^{-\alpha} \tag{8}$$

where $d(x_i, x_j)$ is the Euclidean distance between two points, l is a length-scale parameter and α is a scale mixture parameter. The values of $l = 6.28$ and $\alpha = 0.00248$ are obtained using the L-BFGS-B optimization algorithm (Byrd *et al.*, 1995) implemented in the Python SciPy library (Virtanen *et al.*, 2020).

The obtained surrogate model achieves a mean-squared-error of only 0.04% for L_{long} across 50 test samples, suggesting good agreement with the FE model, as shown in Figure 5. This level of accuracy is sufficient for the present study, because small estimation errors have a negligible effect on the intended behavior. In particular, because electromagnetic emissions are typically characterized on a logarithmic scale, and thus minor deviations do not significantly affect the overall predictive reliability of the model. Moreover, the surrogate model can estimate L_{long} within milliseconds, reducing the computational cost by more than three orders of magnitude compared to the original FE simulations.

In the following section, this surrogate model for L_{long} is combined with the analytical expressions for L_{base} from (1) and $P_{\text{core, loss}}$ from (2) to formulate a MOO problem.

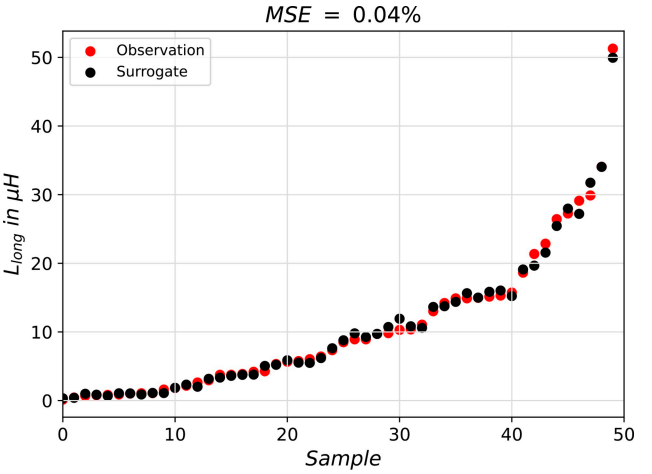

Figure 5. Comparison of FE model and surrogate model for all test samples

Optimization results

The objective of the MOO problem presented in this paper is to identify coupled inductor designs that meet the required constraints on power and longitudinal inductance while minimizing total volume. Therefore, the MOO is solved for:

$$\min \; P_{\text{core, loss}}(\mathbf{x}) \tag{9}$$

$$\min \; V_{\text{core}}(\mathbf{x}) \tag{10}$$

$$\max \; L_{\text{long}}(\mathbf{x}) \tag{11}$$

subject to:

$$P_{\text{core, loss}} \leq 20\,\text{W} \tag{12}$$

$$L_{\text{long}} \geq 10\,\mu\text{H} \tag{13}$$

$$x_0 \leq 30\,\text{mm} \tag{14}$$

$$x_1 \leq 40\,\text{mm} \tag{15}$$

$$x_2 \leq 25\,\text{mm} \tag{16}$$

$$J_{\text{cu}} \leq 10\,\text{A/m}^2 \tag{17}$$

using NSGA-II, implemented in the Python pymoo library (Blank and Deb, 2020). The constraints on $P_{\text{core, loss}}$ and J_{cu} have been defined based on experience gained from previous preliminary prototypes. The constraint on L_{long} was derived from system-level EMI simulations reported in Hussain *et al.* (2025). The geometric constraints on x_0, x_1 and x_2 were arbitrarily selected to exclude designs that are difficult to manufacture and to prevent the design space from expanding to impractically large configurations. The constraint J_{cu} describes the maximal allowed current density within the coil and it is defined as:

$$J_{\text{cu}} = \frac{x_3 I_{\text{DC}}}{k\left(x_0^2 - (x_0 - x_4)^2\right) x_5 \pi / 360} \tag{18}$$

where $k = 0.5$ accounts for the coil's fill factor. The parameter $I_{\text{DC}} = 90\,\text{A}$ is the maximum load current through the coil, determined by the maximum power rating of the converter (here 120 kW 3-phase multilevel interleaved power converter, see Figure 1).

The resulting Pareto front, together with the corresponding input parameters **x** and the convergence behavior, is shown in Figure 6. The Pareto front was obtained using a population size of 5,000 individuals over 100 generations, with a total optimization time of approximately 7 min. As illustrated in Figure 6(a), a wide range of designs satisfies the optimization problem defined in (9)–(17), clearly demonstrating the trade-offs between core

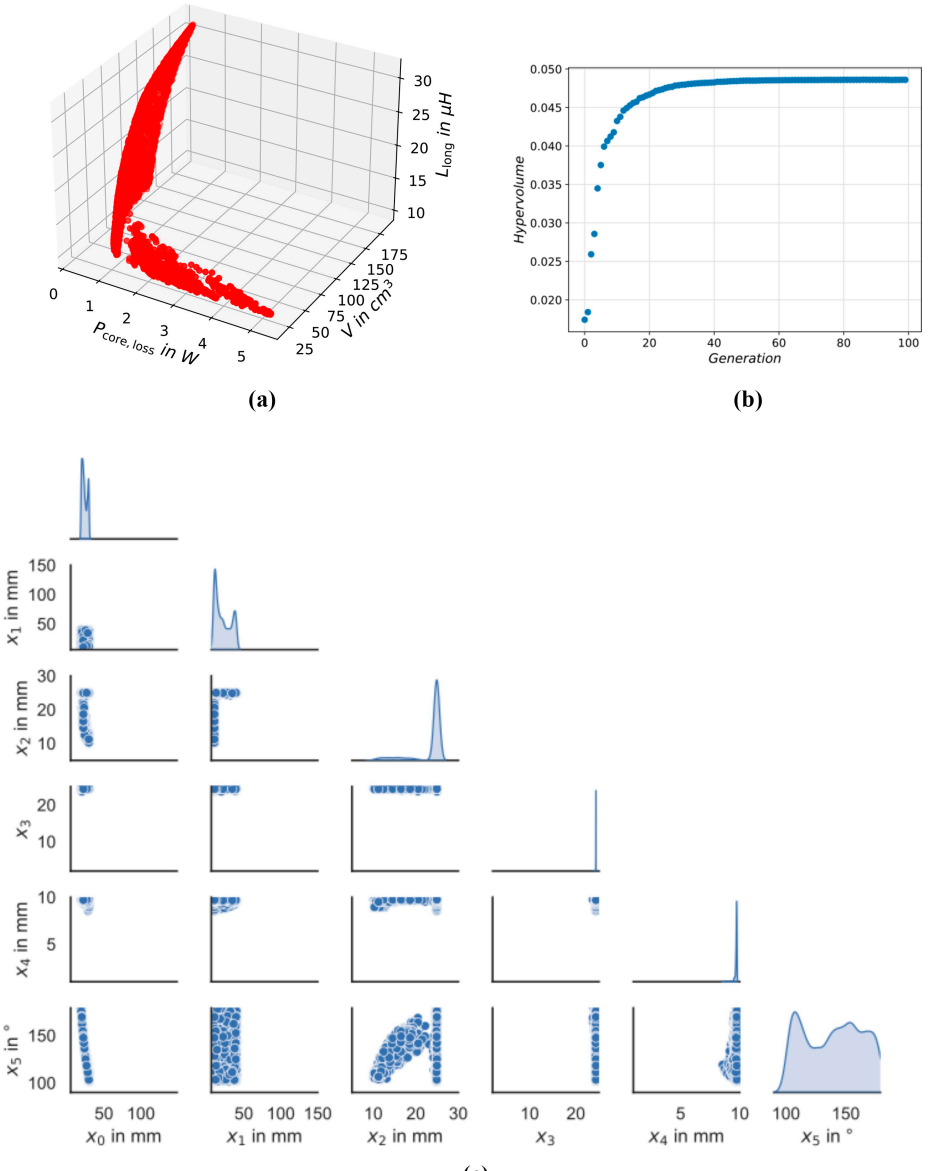

(a) **(b)** **(c)**

Figure 6. (a) Pareto front obtained from the surrogate-based optimization; (b) convergence behavior of MOO process using the hypervolume performance indicator available in Pedregosa *et al.* (2011).The total optimization time requires approximately 7 min using a population size of 5,000 individuals over 100 generations. (c) scatter matrix of the input parameter combinations corresponding to the Pareto-optimal solutions shown in (a)

losses, volume and longitudinal inductance. The volumes of the Pareto-optimal solutions span from 22 to 311 cm^3, indicating significant potential for space reduction in practical applications. Core losses range from 0.25 to 5.3 W, highlighting opportunities to reduce losses and thereby relax cooling requirements. The longitudinal inductance varies from 10 to 31.2 µH, demonstrating the potential to enhance EMI filtering performance when required.

Figure 6(b) shows the convergence behavior of the MOO, evaluated using the hypervolume performance indicator (Pedregosa *et al*., 2011). The hypervolume is computed based on objective values normalized to the range [0,1], enabling a scale-independent assessment of convergence. An increasing hypervolume value over successive generations indicates progressive improvement in both convergence toward the Pareto front and diversity among the solutions.

Finally, Figure 6(c) summarizes the scatter matrix of the input parameter combinations corresponding to the Pareto-optimal solutions shown in (a). As illustrated, multiple feasible solutions exist for the parameters x_0, x_1, x_2 and x_5, whereas only marginal variation is observed for x_3 and x_4. The main diagonal of the scatter matrix displays the probability density functions of the individual design parameters **x**, while the off-diagonal elements depict the joint variation between pairs of parameters, thereby revealing correlations and dependencies within the Pareto-optimal set.

Three Pareto-optimal solutions from Figure 6 are summarized in Table 3, along with their respective input parameters **x**. These solutions highlight the balance between functional performance and cost efficiency. For comparison, Table 3 also includes a reference design manufactured by VAC (Vacuumschmelze, 2025) with a power rating of 120 kW, enabling a comparative assessment of core losses, volume, longitudinal inductance and cost.

Finally, Table 4 compares the longitudinal inductance L_{long} predicted by the surrogate model with the values obtained from the FE model. The relative error remains below 3.4%, confirming the surrogate model's accuracy. To illustrate the differences in size and volume among the three Pareto-optimal solutions in Table 3, their corresponding FE models are shown in Figure 7, scaled by a factor of 4.

Table 3. Three distinct Pareto-optimal solutions are identified, representing trade-offs between minimal core losses, minimal volume and maximal longitudinal inductance

Design parameter	Minimal core losses	Minimal volume	Maximal longitudinal inductance	Reference design
$P_{core,\,loss}$	0.25 W	4.6 W	0.32 W	8 W
V_{core}	245 cm^3	22 cm^3	311 cm^3	116 cm^3
L_{long}	12.1 µH	10.1 µH	31.2 µH	13 µH
x_0	19.2 mm	27.1 mm	30 mm	27 mm
x_1	39.9 mm	10.2 mm	39.8 mm	20 mm
x_2	25 mm	10.7 mm	25 mm	25 mm
x_3	24	24	24	20
x_4	9.74 mm	9.75 mm	9.6 mm	9 mm
x_5	178°	115°	104°	160°
Relative costs	1.6	0.8	1.7	1

Note(s): For comparison also the reference design is shown in the table. The relative cost information given in this table was provided by VAC (Vacuumschmelze, 2025)

Table 4. Difference of L_{long} between surrogate model and FE model for the three Pareto-optimal solutions shown in Table 3

Design case	Surrogate model	FE model	Rel. error (%)
L_{long} at minimal core losses	12.1 µH	11.7 µH	3.4
L_{long} at minimal volume	10.1 µH	10.01 µH	0.9
L_{long} at maximal longitudinal inductance	31.2 µH	30.25 µH	3.1

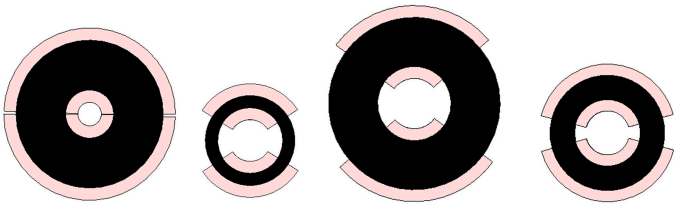

Figure 7. FE models corresponding to the three Pareto-optimal solutions for (a) minimal core losses, (b) minimal volume and (c) maximal longitudinal inductance and (d) FE model of the reference design

Discussion

The design for minimal core losses ($P_{core,\,loss}$ = 0.25 W) achieves the lowest loss, but at the expense of a large core volume (V_{core} = 245 cm^3), approximately double that of the reference. The increased magnetic material reduces the core losses, yet drives up cost by 60% compared to the reference design. In contrast, the minimal-volume design (V_{core} = 22 cm^3) reduces the used material by an order of magnitude but results in substantially higher core losses (4.6 W). The maximal-inductance design yields the highest longitudinal inductance (L_{long} = 31.2 µH), more than twice compared to the reference design. Achieving this requires an even higher core volume (311 cm^3), which again increases material cost by 70%.

The cost analysis highlights a clear trade-off: designs optimized for low losses or high longitudinal inductance demand greater material and manufacturing effort, while the compact configuration minimizes cost only by compromising magnetic efficiency and inductive capability. It is important to note that the core material was not included as a design variable in the optimization process, the relative permeability was therefore held constant. Future investigations may consider alternative core materials to further explore this design space.

In practice, the optimal solution is determined not only by application-specific constraints such as allowable temperature rise, geometric footprint and inductance requirements, but also by the manufacturability of the Pareto-optimal designs. Realizing the proposed configurations generally necessitates multiturn and multilayer winding arrangements, which are known to increase leakage inductance and reduce core utilization, thereby complicating the winding process and introducing additional parasitic effects. To ensure design reliability, a comprehensive winding model that accurately captures turn distribution and magnetic coupling effects is required. Moreover, winding capacitance has not been considered in this work. In high-frequency operation, this parasitic element can significantly influence resonant behavior and EMI characteristics. Similarly, the thermal behavior of the designs is not yet included; because higher core losses or compact configurations can result in elevated

temperatures, future work should include detailed thermal–electromagnetic coupling to evaluate practical limits.

The choice of conductor type has also a significant influence on both manufacturability and electromagnetic performance. In this study, a defined filling factor is assumed to represent the effective packing density of the windings. In practice, however, different designs may use alternative winding technologies – such as round-wire windings (potentially connected in parallel), foil windings or shell-type configurations – each characterized by distinct filling factors. These variations directly affect achievable packing density, thermal dissipation and AC loss behavior. The volume footprint of the designs also remains a critical consideration for integration into constrained assemblies. While the minimal-volume solution achieves the smallest footprint, its higher losses may necessitate additional cooling or spacing, offsetting the initial size advantage. Consequently, the results presented provide a quantitative and practical basis for selecting a balanced design, while emphasizing the need to extend future optimization studies to include winding layout, parasitic capacitance and coupled thermal–electromagnetic behavior for a more comprehensive assessment of performance and reliability.

Conclusion

This paper has presented a multiobjective optimization framework for the design of a coupled inductor used in multilevel interleaved power converter, targeting minimization of core losses (power density constraints), volume (cost considerations) and maximization of longitudinal inductance (EMI performance). The approach combines analytical considerations with a surrogate model trained on 2.5D FE simulations, to significantly reducing the computational burden of the optimization process. The resulting Pareto-optimal designs were validated against FE simulations and demonstrated a relative error of less than 3.4%, thereby confirming the accuracy of the surrogate model. Overall, the proposed framework supports application-specific inductor optimization and can be readily extended to include manufacturability and cost models, thereby bridging performance-driven and economically constrained design objectives.

Acknowledgements

The authors would like to express their sincere gratitude to Vacuumschmelze for providing the material data for their nanocrystalline cores and for sharing their valuable expertise. This work has been jointly supported by Vacuumschmelze GmbH & Co. KG, Hanau, Germany, AVL List GmbH, Graz, Austira, CBMM Technology Suisse SA, Geneve Switzerland and by Silicon Austria Labs (SAL), owned by the Republic of Austria, the Styrian Business Promotion Agency (SFG), the federal state of Carinthia, the Upper Austrian Research (UAR), Industry and the Austrian Association for the Electric and Electronics (FEEI).

References

Abarzadeh, M., Mosaddegh, H., Khoshhava, M.A., Babaie, M., Caron, S. and Al-Haddad, K. (2023), "Systematic design approach for airgap-less hybrid integrated coupled inductor for interleaved paralleled inverters using finite element analysis", in '2023 IEEE Transportation Electrification Conference and Expo (ITEC)', pp. 1-6.

Anderson, J.A., Schrittwieser, L., Leibl, M. and Kolar, J.W. (2017), "Multi-level topology evaluation for ultra-efficient three-phase inverters", in '2017 IEEE International Telecommunications Energy Conference (INTELEC)', pp. 456-463.

Arruti, A., Anzola, J., Pérez-Cebolla, F.J., Aizpuru, I. and Mazuela, M. (2023), "The composite improved generalized steinmetz equation (cigse): an accurate model combining the composite waveform hypothesis with classical approaches", *IEEE Transactions on Power Electronics*, Vol. 39 No. 1, pp. 1162-1173.

Blank, J. and Deb, K. (2020), "Pymoo: multi-objective optimization in python", *IEEE Access*, Vol. 8, pp. 89497-89509.

Boillat, D.O., and Kolar, J.W. (2012), "Modeling and experimental analysis of a coupling inductor employed in a high performance ac power source", *in 2012 International Conference on Renewable Energy Research and Applications (ICRERA)*, pp. 1-18.

Byrd, R.H., Lu, P., Nocedal, J. and Zhu, C. (1995), "A limited memory algorithm for bound constrained optimization", *SIAM Journal on Scientific Computing*, Vol. 16 No. 5, pp. 1190-1208.

Cheng, M., Qin, W., Zhu, X. and Wang, Z. (2022), "Magnetic-inductance: concept, definition, and applications", *IEEE Transactions on Power Electronics*, Vol. 37 No. 10, pp. 12406-12414.

Dassault Systèmes (2025), "CST studio suite, electromagnetic field simulation software", available at: www.3ds.com/products-services/simulia/products/cst-studio-suite/?utm_source=cst.com&utm_medium=301&utm_campaign=cst (Accessed 29April 2025).

Forrester, A.I.J., Sobester, A. and Keane, A.J. (2008), *Engineering Design via Surrogate Modelling – A Practical Guide*, 1st ed. Wiley, Chichester, UK, available at: https://onlinelibrary.wiley.com/doi/book/10.1002/9780470770801

Górecki, K. and Detka, K. (2023), "Spice-aided models of magnetic elements—a critical review", *Energies*, Vol. 16 No. 18, available at: www.mdpi.com/1996-1073/16/18/6568

Hufschmied, G. (2020), *Grundlagen Der Elektrotechnik*, 15th ed. Springer-Verlag GmbH, Heidelberg, Germany.

Hurley, G., Ouyang, Z., Acero, J. and Duffy, M. (2025), "Tutorial lecture on, passives in power electronics: magnetic component design and simulation", ECPE Tutorial, Cambridge, UK.

Hussain, M., Hackl, H., Berger, H., and Auinger, B. (2025), "Computational framework to assess emi of grid-connected inverters as function of topology and pwm scheme", *in '2025 International Symposium on Electromagnetic Compatibility – EMC Europe'*, pp. 102-107.

Mirza, A.B., Emon, A.I., Vala, S.S. and Luo, F. (2023), "An e-core based integrated coupled inductor for interleaved boost converter", *IEEE Transactions on Industry Applications*, Vol. 59 No. 4, pp. 4199-4214.

Mohammed, S.A.Q. and Jung, J.-W. (2021), "A state-of-the-art review on soft-switching techniques for dc–dc, dc–ac, ac–dc, and ac–ac power converters", *IEEE Transactions on Industrial Informatics*, Vol. 17 No. 10, pp. 6569-6582.

Möreé, G. and Leijon, M. (2024), "Iron loss models: a review of simplified models of magnetization losses in electrical machines", *Journal of Magnetism and Magnetic Materials*, Vol. 609, p. 172163.

Oliveri, A., Lodi, M. and Storace, M. (2022), "Nonlinear models of power inductors: a survey", *International Journal of Circuit Theory and Applications*, Vol. 50 No. 1, pp. 2-34.

Paul, C.A. (2006), *Introduction to Electromagnetic Compatibility*, John Wiley and Sons, Inc, New York, NY, United States of America.

Pedregosa, F., Varoquaux, G., Gramfort, A., Michel, V., Thirion, B., Grisel, O., Blondel, M., Prettenhofer, P., Weiss, R., Dubourg, V. and Vanderplas, J. (2011), "Scikit-learn: machine learning in python", *The Journal of Machine Learning Research*, Vol. 12, pp. 2825-2830.

Rashid, M. H., (Ed) (2024), *Power Electronics Handbook*, 5th Ed. Butterworth-Heinemann, Oxford, United Kingdom.

Vacuumschmelze (2025), "Emc products based on nanocrystalline vitroperm", available at: https://vacuumschmelze.de/03_Documents/Brochures/EMC%20Products%20based%20on%20Nanocrystalline%20VITROPERM.pdf. (Accessed 29April 2025).

Virtanen, P., Gommers, R., Oliphant, T.E., Haberland, M., Reddy, T., Cournapeau, D., Burovski, E., Peterson, P., Weckesser, W., Bright, J., van der Walt, S.J., Brett, M., Wilson, J., Millman, K.J., Mayorov, N., Nelson, A.R.J., Jones, E., Kern, R., Larson, E., Carey, C.J., Polat, Feng, Y., Moore, E.W., VanderPlas, J., Laxalde, D., Perktold, J., Cimrman, R., Henriksen, I., Quintero, E.A., Harris, C.R., Archibald, A.M., Ribeiro, A.H., Pedregosa, F. and van Mulbregt, P., İ (2020), "SciPy 1.0: fundamental algorithms for scientific computing in python", *Nature Methods*, Vol. 17 No. 3, pp. 261-272.

Zhang, D., Wang, F., Burgos, R., Lai, R. and Boroyevich, D. (2010), "Impact of interleaving on ac passive components of paralleled three-phase voltage-source converters", *IEEE Transactions on Industry Applications*, Vol. 46 No. 3, pp. 1042-1054.

Appendix

Error of the Classical Steinmetz Equation for Triangular Excitation.

The classical Steinmetz equation (SE) expresses the specific core loss P_v under sinusoidal flux excitation as Arruti *et al.* (2023):

$$P_{v,\mathrm{SE}} = k_{\mathrm{SE}} f^{\alpha} \widehat{B}^{\beta}, \tag{19}$$

where f is the excitation frequency, $\widehat{B}$ is the peak flux density and k_{SE}, α and β are empirical Steinmetz parameters obtained from sinusoidal loss measurements.

The improved generalized Steinmetz equation (iGSE) extends this model to arbitrary periodic waveforms $B(t)$ with period T Arruti *et al.* (2023):

$$P_{v,\mathrm{iGSE}} = \frac{1}{T}\int_0^T k_i \left|\frac{\mathrm{d}B(t)}{\mathrm{d}t}\right|^{\alpha} (\Delta B)^{\beta-\alpha}\,\mathrm{d}t, \tag{20}$$

where $\Delta B = B_{max} - B_{\min}$ is the peak-to-peak flux swing and k_i is an effective loss coefficient that is related to k_{SE}, α and β by enforcing that (19) and (20) coincide for a pure sinusoidal waveform. Let us consider a sinusoidal flux:

$$B_{\sin}(t) = \widehat{B}\,\sin(\omega t), \quad \omega = 2\pi f, \tag{21}$$

with peak-to-peak swing $\Delta B = 2\widehat{B}$. Its time derivative is:

$$\frac{\mathrm{d}B_{\sin}(t)}{\mathrm{d}t} = \omega\widehat{B}\,\cos(\omega t). \tag{22}$$

Substituting this into (20) yields:

$$P^{(\sin)}_{v,\mathrm{iGSE}} = \frac{1}{T}\int_0^T k_i |\omega\widehat{B}\cos(\omega t)|^{\alpha} (2\widehat{B})^{\beta-\alpha}\,\mathrm{d}t \tag{23}$$

$$= k_i\,\omega^{\alpha}\widehat{B}^{\beta} 2^{\beta-\alpha} \cdot \frac{1}{T}\int_0^T |\cos(\omega t)|^{\alpha}\,\mathrm{d}t. \tag{24}$$

With the change of variables $\theta = \omega t$, $T = 2\pi/\omega$, we obtain:

$$\frac{1}{T}\int_0^T |\cos(\omega t)|^\alpha \, \mathrm{d}t = \frac{1}{2\pi}\int_0^{2\pi} |\cos\theta|^\alpha \, \mathrm{d}\theta = C_\alpha, \tag{25}$$

where:

$$C_\alpha = \frac{1}{2\pi}\int_0^{2\pi} |\cos\theta|^\alpha \, \mathrm{d}\theta = \frac{2}{\pi}\int_0^{\pi/2} \cos^\alpha\theta \;\; \mathrm{d}\theta. \tag{26}$$

Thus:

$$P_{\mathrm{v,iGSE}}^{(\mathrm{sin})} = k_\mathrm{i}\, C_\alpha\, 2^{\beta-\alpha}\, (2\pi f)^\alpha\, \widehat{B}^\beta. \tag{27}$$

Requiring consistency with the classical SE equation (19):

$$P_{\mathrm{v,SE}} = P_{\mathrm{v,iGSE}}^{(\mathrm{sin})} \Rightarrow k_\mathrm{SE} f^\alpha \widehat{B}^\beta = k_\mathrm{i}\, C_\alpha\, 2^{\beta-\alpha}\, (2\pi f)^\alpha\, \widehat{B}^\beta, \tag{28}$$

gives the relationship:

$$k_\mathrm{i} = \frac{k_\mathrm{SE}}{C_\alpha\, 2^{\beta-\alpha}(2\pi)^\alpha}. \tag{29}$$

Next, we consider a symmetric triangular flux waveform with the same period T and peak value $\widehat{B}$ as the sinusoid. Over one period, $B_\mathrm{tri}(t)$ ramps linearly from $-\widehat{B}$ to $+\widehat{B}$ in $T/2$ and back to $-\widehat{B}$ in the remaining $T/2$, so the magnitude of the slope is constant:

$$\left|\frac{\mathrm{d}B_\mathrm{tri}(t)}{\mathrm{d}t}\right| = \frac{4\widehat{B}}{T} = 4\widehat{B}f, \tag{30}$$

and the peak-to-peak swing is again $\Delta B = 2\widehat{B}$. Inserting this into (20) yields:

$$P_{\mathrm{v,iGSE}}^{(\mathrm{tri})} = \frac{1}{T}\int_0^T k_\mathrm{i} \left|\frac{\mathrm{d}B_\mathrm{tri}(t)}{\mathrm{d}t}\right|^\alpha (2\widehat{B})^{\beta-\alpha}\, \mathrm{d}t \tag{31}$$

$$= k_\mathrm{i}\, \left(4\widehat{B}f\right)^\alpha\, (2\widehat{B})^{\beta-\alpha} \tag{32}$$

$$= k_\mathrm{i}\, 4^\alpha 2^{\beta-\alpha} f^\alpha \widehat{B}^\beta. \tag{33}$$

Using $4^\alpha = 2^{2\alpha}$, this simplifies to:

$$P_{\mathrm{v,iGSE}}^{(\mathrm{tri})} = k_\mathrm{i}\, 2^{\beta+\alpha} f^\alpha \widehat{B}^\beta. \tag{34}$$

Substituting k_i from (29) gives:

$$P_{\mathrm{v,iGSE}}^{(\mathrm{tri})} = \frac{k_{\mathrm{SE}}}{C_\alpha\, 2^{\beta-\alpha}(2\pi)^\alpha}\, 2^{\beta+\alpha} f^\alpha \widehat{B}^\beta \tag{35}$$

$$= k_{\mathrm{SE}} f^\alpha \widehat{B}^\beta \frac{2^{2\alpha}}{C_\alpha (2\pi)^\alpha}. \tag{36}$$

Therefore, the ratio between the iGSE prediction for triangular excitation and the SE prediction (which corresponds to sinusoidal calibration) is:

$$\frac{P_{\mathrm{v,iGSE}}^{(\mathrm{tri})}}{P_{\mathrm{v,SE}}} = \frac{2^{2\alpha}}{C_\alpha (2\pi)^\alpha}, \tag{37}$$

where $P_{\mathrm{v,SE}} = k_{\mathrm{SE}} f^\alpha \widehat{B}^\beta$ as in (19). Note that the exponent β cancels out in the ratio; the deviation depends only on α.

For the parameters used in this work, $\alpha = 1.51$ and $\beta = 2.4$, the constant C_α defined in (26) evaluates numerically to:

$$C_\alpha \approx 0.555. \tag{38}$$

Inserting this into (37) yields:

$$\frac{P_{\mathrm{v,iGSE}}^{(\mathrm{tri})}}{P_{\mathrm{v,SE}}} \approx \frac{2^{2\cdot 1.51}}{0.555\ (2\pi)^{1.51}} \approx 0.911. \tag{39}$$

Hence, for a symmetric triangular flux waveform with the same peak value $\widehat{B}$ and frequency f as the sinusoidal excitation used to identify the Steinmetz parameters, the classical SE overestimates the core loss by approximately:

$$\frac{P_{\mathrm{v,SE}} - P_{\mathrm{v,iGSE}}^{(\mathrm{tri})}}{P_{\mathrm{v,iGSE}}^{(\mathrm{tri})}} \approx \frac{1}{0.911} - 1 \approx 9.8\%. \tag{40}$$

This shows that, for $\alpha = 1.51$ and $\beta = 2.4$, the modeling error introduced by using the classical SE for symmetric triangular excitation is on the order of 10%, with the SE providing a conservative (slightly pessimistic) estimate of the core loss.

Corresponding author
Christian Riener can be contacted at: christian.riener@silicon-austria.com